Modelling and
Simulation in Materials
Science and
Engineering

ACCEPTED MANUSCRIPT

Atomistic simulation of HF diffusion on ammonium fluorosilicate surface using neural network potential

To cite this article before publication: Hyungmin An *et al* 2025 *Modelling Simul. Mater. Sci. Eng.* in press https://doi.org/10.1088/1361-651X/add283

Atomistic simulation of HF diffusion on ammonium fluorosilicate surface using neural network potential

Hyungmin An[1]‡, Jisu Kim[1]‡, Gijin Kim[1], Seungwu Han[1,2]§

[1] Department of Materials Science and Engineering, Seoul National University, Seoul, 08826, Korea

[2] Korea Institute for Advanced Study, AI center, Seoul, 02455, Korea

E-mail: hansw@snu.ac.kr

December 2024

Abstract. Plasma etching is an essential technology in semiconductor fabrication, enabling precise nanoscale patterning. For high-aspect-ratio channel hole etching in 3D NAND flash memory, cryogenic etching using hydrogen fluoride (HF) gas shows great potential. This process often leads to the deposition of ammonium hexafluorosilicate (AFS) on sidewalls, which critically impacts surface diffusion. Understanding such phenomena requires accurate atomistic modeling, and while density functional theory (DFT) provides reliable and accurate results, its significant computational cost makes it challenging to apply to large-scale or dynamic simulations. As a promising alternative, neural network potentials (NNPs) provide DFT-level accuracy at a fraction of the computational cost. In this study, we develop a fine-tuned NNP based on the pretrained SevenNet-0 model to simulate HF diffusion on AFS surfaces. Although SevenNet-0 is trained on a broad chemical space and exhibits great generalization capabilities, it requires further refinement to accurately capture the complex energy landscape occurring during cryogenic etching, particularly for configurations far from equilibrium. To address this, we fine-tune the SevenNet-0 model using a minimal DFT dataset. The resulting fine-tuned NNP demonstrates superior accuracy and stability in molecular dynamics simulations compared to both the NNP trained from scratch and the SevenNet-0 model. Our analysis reveals that the additive gas IF_5 enhances HF diffusivity by reducing chain formation and lowering the diffusion barrier. This work underscores the potential of fine-tuned NNPs for simulating complex etching processes, offering valuable insights for advancing semiconductor manufacturing.

1. INTRODUCTION

Plasma etching has become a cornerstone technology in semiconductor fabrication, especially as the demand for device miniaturization and high integration continues to grow. The growing needs led to the introduction of reactive ion etching (RIE), a technique that enables anisotropic etching by leveraging ions, which precisely remove

‡ H.A. and J.K. contributed equally to this paper.

§ Corresponding author. hansw@snu.ac.kr

material in the vertical direction, and radicals, which facilitate selective chemical reactions. These advancements in plasma etching have driven the development of nanoscale patterning and high aspect-ratio etching. [1, 2, 3]

One of the most critical applications of plasma etching is in 3D NAND flash memory fabrication, particularly during the channel hole etching step, where alternating silicon oxide (SiO_2) and silicon nitride (SiN_x) layers are etched with high precision and depth [4, 5]. The depth of these etched channel holes directly determines the stack height of NAND flash and integration density. As the aspect ratio of these channel holes increases, significant issues arise such as profile deformation and reduced etch rates caused by aspect ratio dependent etching (ARDE), which can negatively affect process efficiency and reliability [6, 7, 1].

Cryogenic etching, also known as low-temperature etching, has been introduced as a potential solution to such challenges in plasma etching [8, 9, 10, 11, 12]. Enhanced etch characteristics of cryogenic etching have been attritubted to two critical aspects of channel hole etching: chemical reaction at the etch front and neutral transport on the sidewall. At the etch front, low temperatures reportedly enhance the physisorption of etchants or reaction catalysts, thereby accelerating chemical reactions [13, 14, 9, 15, 10]. Despite the reduced thermal energy under cryogenic conditions, which decreases the occurrence of chemical reactions, the kinetic energy of radicals and ions generated in the plasma can still enhance reactivity, as previous studies suggested [16]. On the sidewall, cryogenic conditions improve both Knudsen transport and surface diffusion, with the latter likely dominating as the primary transport mechanism in profiles with small feature sizes [16]. Indeed, lowering the substrate temperature below 0 °C has been shown to improve the etch rate of SiO_2 during the fabrication of the channel hole [10]. Furthermore, transitioning from fluorocarbon (CF_x)-based gases to hydrogen fluoride (HF) gas as the etchant under these cryogenic conditions has demonstrated even greater improvements in etch efficiency [17, 12].

Experimental and computational studies have shown that during etching with HF, byproducts such as ammonia (NH_3) and silicon tetrafluoride (SiF_4) react to form ammonium hexafluorosilicate ($(NH_4)_2SiF_6$, AFS), which deposits on the sidewall surface [18, 19, 20, 12]. AFS is known to be highly stable under cryogenic conditions, resisting decomposition and altering the surface diffusion characteristics. Also, additive gases such as iodine pentafluoride (IF_5) may also be used to enhance cryogenic etching characteristics [21]. Despite these facts, experimental studies on cryogenic etching remain underdeveloped, largely due to the technical challenges of operating under cryogenic conditions and the limitations of current measurement equipment.

To overcome these experimental limitations, studies utilizing computational simulations have been conducted. Related research includes modeling the role of physisorption under cryogenic conditions [22], profiling simulation of cryogenic etching processes [23, 24], and exploring neutral transport associated with ARDE in high-aspect-ratio structures [25, 26, 27]. While there are a few studies on low-temperature etching from an atomistic perspective [13], further research in this area remains necessary.

For atomistic modeling of surface systems like AFS surfaces, computational simulations often employ density functional theory (DFT). However, DFT-based simulations of processes such as molecular dynamics (MD) or nudged elastic band (NEB) [28, 29] are computationally prohibitive due to their intensive resource requirements. To address these challenges, neural network potentials (NNPs) have emerged, enabling rapid calculations with high accuracy. Nonetheless, constructing NNPs remains challenging, as the preparation of training datasets must adequately capture interactions among etchants, additives, and surfaces, as well as the configurations that emerge during the etching process.

Recently, pretrained universal NNPs [30, 31, 32, 33] have emerged as a promising solution, significantly reducing the time-intensive process of developing tailored NNPs, which typically involves repeated dataset optimization and extensive experimentation [34]. One of the major advantages of pretrained universal NNPs is their ability to generalize across a wide range of applications with minimal dependency on the specifics of the training dataset. This versatility stems from their training on extensive and diverse datasets, making them applicable to a broad spectrum of systems. However, configurations encountered in cryogenic etching processes can deviate significantly from the equilibrium crystal structures on which pretrained models are usually trained. This discrepancy increases the potential for prediction errors in configurations far from equilibrium, which are commonly observed in cryogenic etching.

To address this challenge, fine-tuning pretrained models using system-specific data has proven to be an effective strategy [35, 36]. Fine-tuning allows the pretrained NNP to adapt to datasets that capture the unique chemical environments and off-equilibrium dynamics characteristic of cryogenic etching. This process enhances the ability of the model to accurately predict key behaviors. By leveraging the computational efficiency of pretrained models while improving their accuracy for specialized systems, fine-tuning significantly reduces both computational costs and development time. Consequently, fine-tuning enables more reliable simulation of cryogenic etching, particularly for investigating diffusion behaviors in these complex processes. Since diffusion is governed by atomic interactions, accurately capturing energy and force is crucial to modeling surface diffusion, especially in cryogenic conditions. Energy determines the stability of diffusing molecules, while force directly influences their movement. Additionally, stress plays a role in ensuring the stability of the simulated surface, which indirectly affects diffusion behavior.

In this study, we focus on atomistic modeling of transport properties of HF etchants during the 3D NAND channel hole etching process. Particularly, we put emphasis on surface diffusion on the sidewall surface due to its critical role in small-feature fabrication. We analyze the effects of key process parameters, including temperature and additive gases, on surface diffusivity. Given the importance of AFS in modifying sidewall properties, our modeling efforts are concentrated on AFS surfaces to provide insights into surface diffusion under realistic etching conditions. Furthermore, by comparing cases with and without IF_5 additive gases, we aim to elucidate their influence on surface

diffusion and overall etching performance. In this work, we specifically investigate IF_5 as an example of an additive gas. While other additive gases are not explicitly tested, the same methodology can be applied to study their effects in future work.

2. Methods

2.1. Pretrained SevenNet-0 model

We utilize SevenNet-0 (version 11July2024 [37]), a pretrained universal NNP trained using the SevenNet [30], which is based on the NequIP [38] architecture, as a starting model for fine-tuning. SevenNet-0 has been trained on the MPtraj dataset from Materials Project database [39, 31] without any splitting, resulting in the model learning an extensive amount of DFT calculation data, encompassing 89 elements, 145,923 materials, and a total of 1,580,395 structures. The hyperparameters of SevenNet-0 are primarily adopted from ref. [30, 40]. The cutoff radius is set to 5 Å, with a complexity based on a maximum degree of spherical harmonics ($l_{\text{max}} = 2$) and five interaction layers. The number of channels for each spherical harmonics degree is set to 128 channels for `0e`, 64 channels for `1e`, and 32 channels for `2e` features. As a result, the model comprises 842,440 trainable model parameters.

SevenNet-0 demonstrates high accuracy with a relatively small number of parameters, as supported by the Matbench Discovery benchmark results [41]. It achieves excellent generalization over a broad chemical space, making it a robust choice for diverse

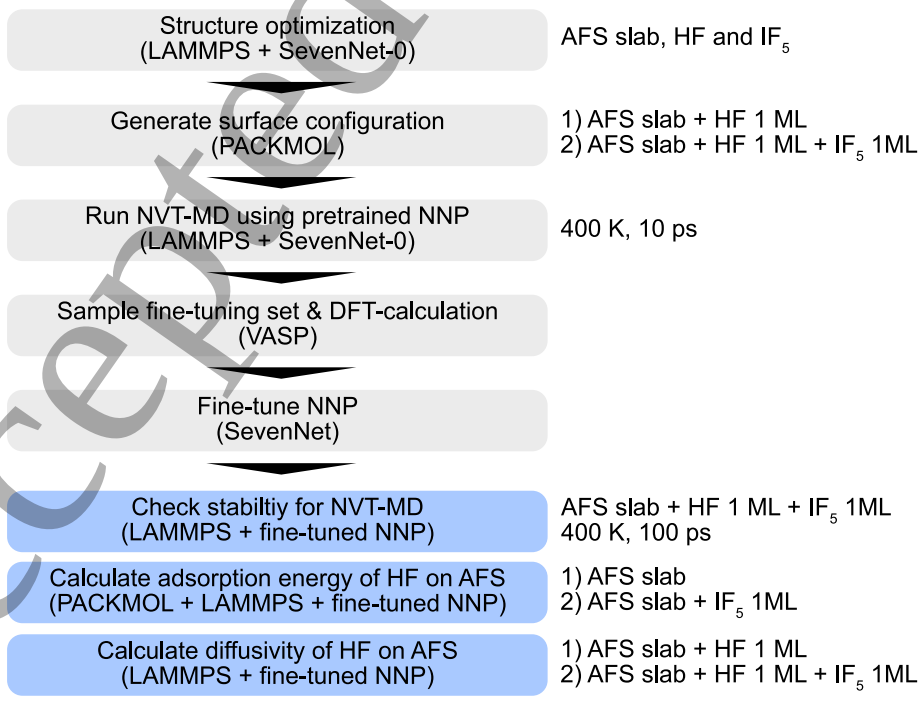

Figure 1. Schematic illustration for the workflow of this study.

applications. The training results show high accuracy, achieving a mean-absoulte-error (MAE) of 11 meV/atom, 41 meV/Å, and 2.78 kB for energy, force, and stress, respectively.

2.2. DFT and NNP calculation

The DFT calculations for this study are performed using the Vienna *ab initio* Simulation Package (`VASP`) [42]. The Perdew-Burke-Ernzerhof (PBE) functional [43] is employed as the exchange-correlation functional, and version 52 of the VASP PBE pseudopotentials is used to ensure compatibility with the pretrained data and to facilitate seamless comparisons with SevenNet-0. Spin-unpolarized calculations are conducted with a plane-wave basis set cutoff energy of 500 eV. For Brillouin zone sampling, Γ-point calculations are performed.

MD simulations and structure relaxation calculations using NNPs, including SevenNet-0, are carried out with the Large-scale Atomic/Molecular Massively Parallel Simulator (`LAMMPS`) [44] and the Atomic Simulation Environment (`ASE`) [45]. SevenNet explicitly incorporates van der Waals interactions through an efficient implementation of Grimme's D3 dispersion correction with Becke-Johnson (BJ) damping [46, 47]. By using this feature, we train the NNP exclusively with the PBE functional database and subsequently apply the D3 correction in atomistic simulation. This approach enables the NNP to achieve results corresponding to the PBE-D3 level of theory calculation. For comparison, DFT calculations are conducted at the same PBE-D3 level with BJ damping for direct comparison with the NNP results. All MD simulations are conducted as NVT simulations using the Nose-Hoover thermostat, with a time step of 1 fs. For structural relaxation, both DFT and NNP calculations consider a structure to be converged to a minimum if the maximum atomic force is less than 0.03 eV/Å.

2.3. Modeling surface diffusion on profile sidewall

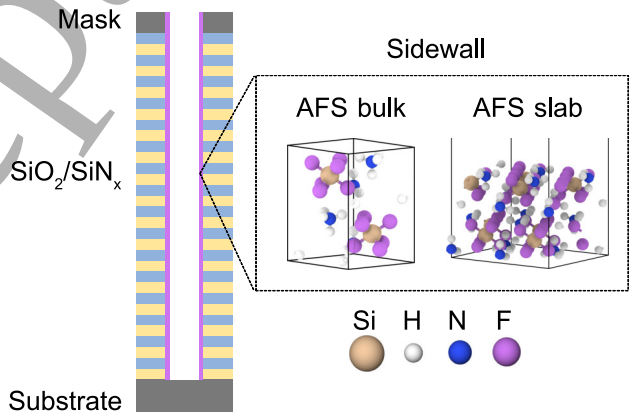

Figure 2. Schematic diagram of channel hole and ammonium hexafluorosilicate (AFS) system on sidewall.

To simulate the surface diffusion behavior of the etchant gas and additive gas on the sidewall during cryogenic etching, we use the crystalline AFS structure (Fig. 2). Experimentally, three phases of AFS have been identified: α (cubic), β (trigonal), and γ (hexagonal) [48, 49, 50]. Although AFS formation has been experimentally confirmed in plasma etching and atomic layer etching processes through XPS spectra [20, 51], the specific AFS phase has not been reported. Since the α and β-phases involve disordered hydrogen atoms bonded to an ammonium ion (NH_4^+), making it difficult to construct a definitive crystal structure, we select the relatively simple γ-phase as our modeling system.

The unit cell of the γ-phase AFS structure consists of 2 fluorosilicate (SiF_6^{2-}) anions and 4 NH_4^+ cations, comprising a total of 34 atoms. From this structure, we construct a slab structure exposing the (001) surface. To achieve this, a 2×2×1 supercell is generated from the unit cell, and a 15 Å vacuum is added to form the slab structure. During structure optimization and molecular dynamics calculations, one bottom layer, approximately 4 Å thick, is fixed to ensure stability.

In the case of inserting gas onto a slab structure, the amount of gas for 1 monolayer (1 ML) is defined as follows. The maximum pair distance between atoms within a molecule is set as the 1 ML thickness. Using the PACKMOL [52] package, the maximum number of molecules that can be inserted within the given tolerance is determined as the 1 ML quantity of the molecule. The tolerance is set to 2.38 Å (first peak of H–H pair), which is the largest value of the first peaks among H–H, H–F, and F–F in the radial distribution function (RDF) obtained from a 10 ps NVT MD simulation of HF liquid at 250 K using SevenNet-0.

3. RESULTS AND DISCUSSION

3.1. Data efficiency of fine-tuning

3.1.1. Fine-tuning SevenNet-0 To fine-tune the pretrained SevenNet-0 model, we generate atomic structures for the training set using SevenNet-0 NVT MD simulations conducted over a short duration of 10 ps at 400 K. We consider two systems: (1) an AFS slab with 1 ML of HF molecules, and (2) an AFS slab with a 1 ML of IF_5 additive gas along with 1 ML of HF molecules. We intentionally set the temperature at 400 K, which is higher than the typical cryogenic etching temperature, to capture diverse and dynamic configurations, enhancing the robustness and accuracy of the fine-tuned model.

From the 10 ps MD trajectories of each system, we sample 51 structures at 200 fs intervals and perform DFT single-point calculations to construct the training set. Additionally, to improve the accuracy of HF molecule physisorption energy predictions, we also include DFT relaxation path trajectory for a single HF molecule, which comprises 6 structures. In total, the training set contains 108 structures. The training set that we prepared is minimal, as our goal is to fine-tune the well-trained SevenNet-0 model, making such a small dataset sufficient for achieving effective fine-tuning.

Fine-tuning starts with the pretrained model parameters of SevenNet-0. Model hyperparameters are all same with pretrained SevenNet-0. A warm-up learning rate scheduler is employed, with a maximum learning rate of 0.0001. The fine-tuning process consists of 400 epochs with Adam optimizer. In this study, we utilize the Huber loss function, the same as used in the training of SevenNet-0, defined in Eq. (1):

$$\mathcal{L}_{\text{Huber}}(\hat{y}, y, \delta) = \begin{cases} \frac{1}{2}(\hat{y} - y)^2, & |\hat{y} - y| \leq \delta, \\ \delta \cdot \left(|\hat{y} - y| - \frac{1}{2}\delta\right), & \text{otherwise.} \end{cases} \tag{1}$$

Here, δ is specified as 0.01. The total loss function incorporates energy, force, and stress contributions as follows in Eq. (2):

$$\begin{aligned} \mathcal{L} = & \frac{1}{M} \sum_{i=1}^{M} \mathcal{L}_{\text{Huber}} \left(\frac{\hat{E}_i}{N_i}, \frac{E_i}{N_i}, \delta \right) \\ & + \frac{\lambda_{\text{F}}}{3M \sum_{i=1}^{M} N_i} \sum_{i=1}^{M} \sum_{j=1}^{N_i} \sum_{k=1}^{3} \mathcal{L}_{\text{Huber}} \left(\hat{F}_{i,j,k}, F_{i,j,k}, \delta \right) \\ & + \frac{\lambda_{\text{S}}}{6M} \sum_{i=1}^{M} \sum_{l=1}^{6} \mathcal{L}_{\text{Huber}} \left(\hat{S}_{i,l}, S_{i,l}, \delta \right). \end{aligned} \tag{2}$$

Here, M represents the number of samples in a batch, and N_i denotes the number of atoms in the i-th sample. The terms E_i, $F_{i,j,k}$, and $S_{i,l}$ correspond to the reference DFT total energy, the k-th component of the atomic force of the j-th atom, and the l-th component of the stress tensor, respectively. Their predicted counterparts, $\hat{E}_i$, $\hat{F}_{i,j,k}$, and $\hat{S}_{i,l}$, are outputs from the NNP model. For loss computation, energy, force, and stress values are expressed in units of eV, eV/Å, and kbar, in that order. The weight parameters λ_{F} and λ_{S} control the contributions of the force and stress terms to the total loss, with values set to 1 and 0.01. Loss function and its parameters are same with those used in the SevenNet-0 training.

To evaluate the data efficiency of fine-tuning, a scratch NNP is also developed for comparison. This baseline model is trained from scratch using the same training data and the same number of 400 epochs. However, due to the high initial error levels typically observed in training from scratch, the learning rate is increased to 0.001 to facilitate faster convergence. In this work, we specifically use a cosine annealing with warm-up scheduler as our learning rate scheduler. This approach starts with an extremely low learning rate (0) and gradually increases it to the maximum learning rate (0.0001 in this study) over the course of 50 epochs. After reaching this peak, the learning rate then gradually decreases back to 0 following a cosine function. Starting from 0 prevents the model's weights from deviating too sharply from the pretrained SevenNet-0 at the beginning of training, ensuring more stable fine-tuning. Fig. 3(a) shows the total training Huber loss of the fine-tuned NNP and the scratch NNP on the training set as a function of epochs. Notably, the scratch NNP trained for 400 epochs exhibits even a higher loss on the training data compared to SevenNet-0. Additionally, the fine-tuned NNP achieves both a significantly smaller loss than the scratch NNP and faster

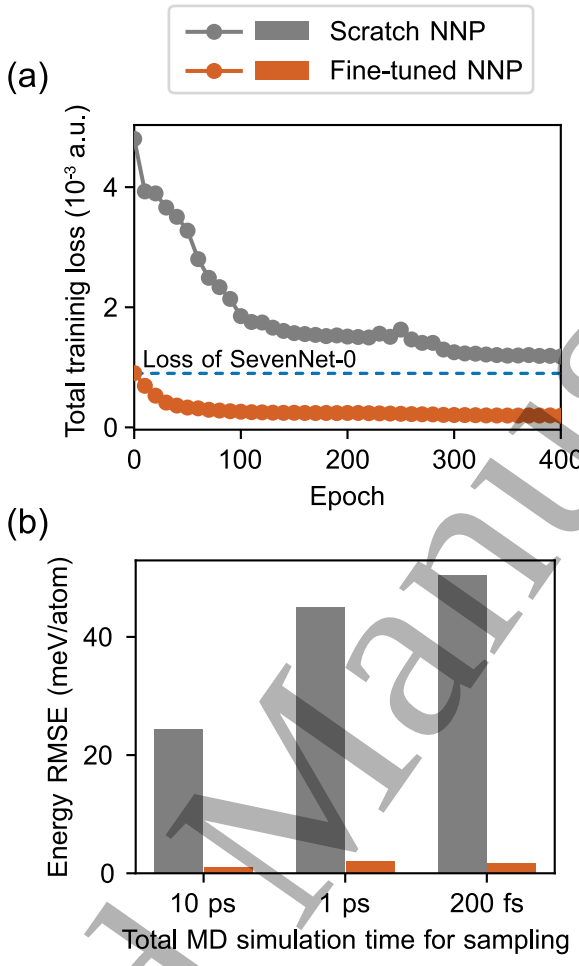

Figure 3. Comparison of the accuracy between scratch NNP and fine-tuned NNP. (a) Training Huber loss per epoch for scratch NNP and fine-tuned NNP trained on a dataset of 108 structures sampled from a 10 ps MD simulation. The blue dashed line represents the Huber loss of SevenNet-0 on the same training set. (b) Energy RMSE on the training set (108 structures sampled from a 10 ps MD simulation) for scratch NNP and fine-tuned NNP, both trained for 400 epochs. The total MD simulation time used for sampling the training dataset is progressively reduced to demonstrate the efficiency of fine-tuned NNP.

loss convergence, demonstrating the efficiency of the fine-tuning approach. Correlation parity plot of fine-tuned NNP can be found in Fig. S4.

We further investigate the efficiency of fine-tuning by reducing the size of the training set sampled from SevenNet-0 MD simulations. Specifically, instead of sampling by 200-fs interval from the full 10 ps trajectory (51 structures from each MD trajectory; total 108 structures), we prepare training sets by shortening the maximum MD simulation time for sampling to 1 ps (6 structures from each MD trajectory; total 18 structures) and 200 fs (2 structures from each trajectory; total 10 structures), respectively. We evaluate the prediction errors of the NNPs trained on the reduced datasets by using a consistent test set composed of 108 structures, which includes

Table 1. Energy, force, and stress RMSE for 108 structures: comparison of NNPs trained on different training set sizes (in units of meV/atom, eV/Å, and kbar).

Total MD time for sampling	Scratch NNP ($E/F/S$)	Fine-tuned NNP ($E/F/S$)
10 ps	24 / 0.41 / 2.10	1 / 0.07 / 0.86
1 ps	45 / 0.73 / 4.28	2 / 0.13 / 1.12
200 fs	50 / 0.96 / 4.58	2 / 0.15 / 1.52

structures sampled from the full 10 ps MD trajectory, as shown in Fig. 3(b). The fine-tuned NNP shows a low energy root-mean-squared error (RMSE) of only 2 meV/atom, even when the total MD simulation time for sampling is drastically reduced to 200 fs. In contrast, the scratch NNP exhibits a significantly higher energy RMSE of 50 meV/atom under the same conditions, highlighting its inability to effectively capture the underlying potential energy surface (PES) with a limited dataset. These results underscore the robustness of fine-tuned NNP, as it consistently achieves low prediction errors across various dataset sizes, while the accuracy of scratch NNP declines significantly as the size of the training set becomes smaller. The detailed errors for energy, force, and stress, expressed in units of meV/atom, eV/Å, and kbar are specified in Table 1. Test set results are also presented in the Table S2.

3.1.2. MD simulation stability analysis We evaluate whether the developed NNPs, including SevenNet-0, can accurately and stably perform MD simulations for analyzing the diffusion behavior of the sidewall during the cryogenic etching process. NVT MD simulations are conducted on a system comprising an AFS slab with 1 ML of IF_5 and 1 ML of HF at 400 K with each developed NNP. To assess stability beyond the 10 ps of simulation time used for training data generation, we perform 100 ps MD simulations.

DFT single-point calculations are performed on the MD simulation trajectories of each NNP to compare their accuracy of predictions. As shown in Fig. 4, the fine-tuned NNP achieves smaller energy errors compared to SevenNet-0, demonstrating improved prediction accuracy for the diffusion process through fine-tuning. In contrast, the scratch NNP fails to perform stable MD simulations, even though the system is explicitly included in its training set. Fig. S1 illustrates the bond lengths of Si–F in SiF_6^{2-} and N–H in NH_4^+ within the AFS slab as a function of MD simulation time. In the case of the fine-tuned NNP, the bond lengths remain consistent without bond breaking, maintaining a stable AFS slab structure. In contrast, for the scratch NNP, Si–F and N–H bonds break within 500 fs, leading to the unphysical collapse of the AFS slab structure. Developing an accurate scratch NNP for complex surface simulations typically requires training sets with both stable and distorted structures of fundamental bulk or molecular systems [53, 54, 55], and the lack of such knowledge explains the instability in this scratch NNP case. The fine-tuned NNP, however, starts training within the parameter space of well-trained SevenNet-0, allowing it to achieve high accuracy for describing

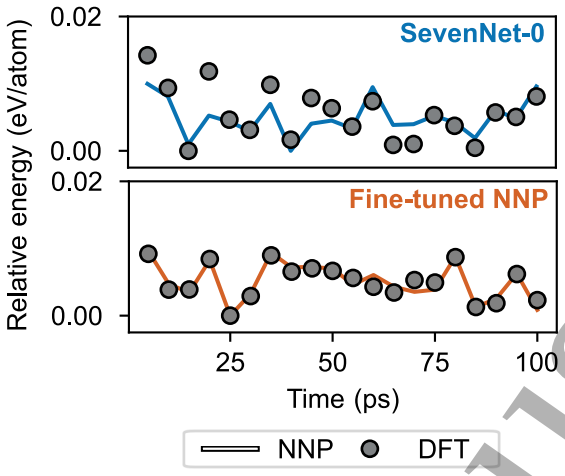

Figure 4. Energy plots of 100 ps of NNP-MD simulations at 400 K for the system of AFS slab with 1 ML of IF_5 and 1 ML of HF molecules. DFT single-point calculations are conducted for each NNP-MD trajectory performed by SevenNet-0 and fine-tuned NNP. We set the most stable structure among the snapshots in each trajectory as the reference with a relative energy of 0 eV/atom.

such complex PES of the diffusion process. Prediction parity plot for SevenNet-0 on the pretrained MPtrj dataset is shown in Fig. S5. This indicates that the pretrained dataset contains a significant number of distorted structures with high energy and high force. Due to the failure of physical simulations with the scratch NNP, it will no longer be included in tests from this point onward.

3.2. NNP assessment for diffusion-related properties

3.2.1. HF physisorption energy From this section, we examine whether fine-tuned NNP achieves improvement in accuracy compared to SevenNet-0 and verify its ability to accurately describe diffusion-related behaviors. To explore the diffusion behavior of the HF molecule, it is essential to accurately describe the physisorption energy. Since the HF molecule continuously undergoes the process of physisorption while diffusing on the surface, diffusion and physisorption energy are directly correlated. If the physisorption energy is too large, the molecule may remain confined to the surface, hindering diffusion. Conversely, if the physisorption energy is too small, the molecule may desorb without any significant interaction with the surface. Thus, having an appropriate physisorption energy is critical. To investigate this, the physisorption energy is calculated using SevenNet-0 and a fine-tuned NNP.

The physisorption energy is evaluated for two systems: (1) AFS slab with a single HF molecule adsorbed, and (2) AFS slab with 1 ML of IF_5 and a single HF molecule adsorbed. For each case, 10 different configurations are generated, and the physisorption energy, E_{phys}, is calculated using the following equation:

$$E_{\mathrm{phys}} = E_{\mathrm{slab+mol}} - (E_{\mathrm{slab}} + E_{\mathrm{molecule}})\,. \tag{3}$$

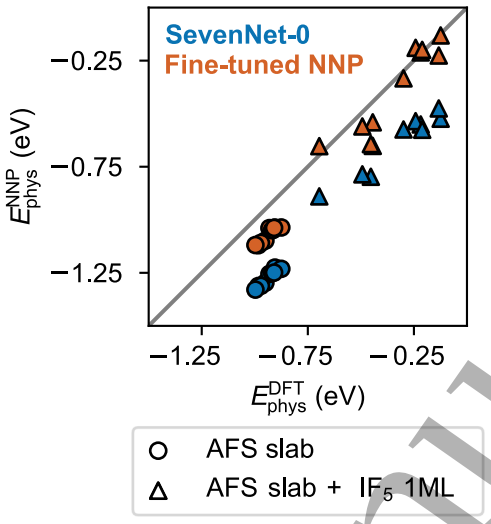

Figure 5. Parity plot comparing the calculated physisorption energy between DFT and both SevenNet-0 and fine-tuned NNP. Blue markers represent the energies from SevenNet-0, while orange markers indicate the energies from the fine-tuned NNP. Circular markers represent cases where a single HF molecule is physisorbed on an AFS slab system. Triangular markers correspond to cases where a single HF molecule is physisorbed on an AFS slab system with an additive gas, specifically 1 ML of IF_5.

As shown in Fig. 5, SevenNet-0 consistently exhibits overbinding behavior, resulting in a MAE of 0.32 eV in E_{phys}. In contrast, the fine-tuned NNP significantly reduces the overbinding issue, achieving an MAE of 0.097 eV in E_{phys}. This demonstrates that the fine-tuning process successfully develops a NNP capable of accurately describing physisorption phenomena. Notably, the physisorption for systems with the additive gas of IF_5 is weaker compared to the systems with only the AFS slab. The impact of this observation on diffusion will be further discussed in the following section.

3.2.2. Diffusivity To calculate the diffusivity of HF molecules, we conduct NVT MD simulations running for 5 ps in the case of DFT and 10 ps for NNP. Calculations are conducted at four temperatures of 250, 300, and 350 K, and five simulations are performed for each temperature. Although cryogenic etching is usually done at temperatures as low as from –20 ℃ to more than –60 ℃ [17, 56, 57, 58], excessively low temperatures may result in sluggish molecular motion, significantly extending the required MD simulation time for diffusivity calculation. Considering these factors, the selected temperature range is deemed appropriate for generating diffusivity plots.

The time-averaged mean squared displacement (MSD) method is employed to enhance sampling density and reduce fluctuations, thereby improving the linearity of the MSD curve. [59] To distinguish the diffusivity of the HF etchant only, bond analysis is conducted on the initial MD snapshot to track only the fluorine atoms belonging to HF. Equation 4 is used, taking into account only x and y components of the displacement

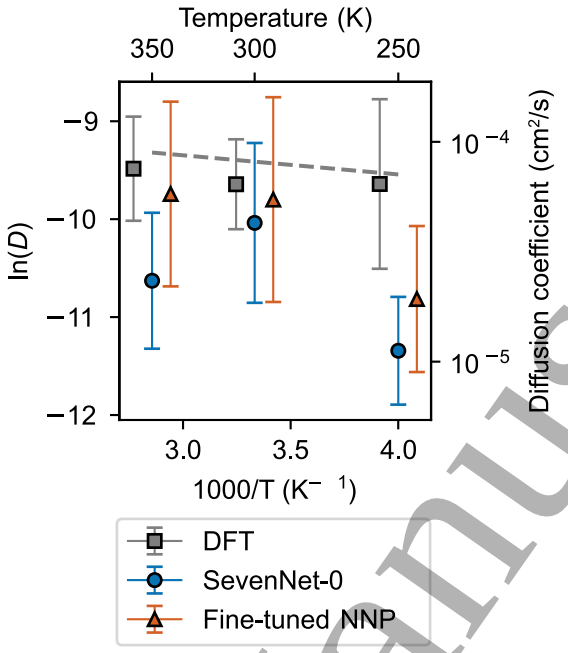

Figure 6. Diffusivity of HF molecules. NVT MD simulations were performed for 10 ps at temperatures of 250, 300, and 350 K, with five simulations conducted at each temperature. Markers represent the average value of $\ln(D)$, while solid lines show the range between the minimum and maximum values. For clarity, results obtained at the same temperature using different potentials (DFT, SevenNet-0, and fine-tuned NNP) are slightly shifted laterally in the diagram. For the DFT results, the grey dashed line represents the temperature dependence of diffusivity, which can be used to calculate the activation energy.

vectors to extract the surface diffusion term.

$$\mathrm{MSD}(\Delta t) = \frac{1}{N}\sum_{i=1}^{N}\frac{1}{N_{\Delta t}}\sum_{t=0}^{t_{\mathrm{tot}}-\Delta t}|\mathbf{r}_{i,\mathrm{xy}}(t+\Delta t)-\mathbf{r}_{i,\mathrm{xy}}(t)|^2 \tag{4}$$

where N is the total number of atoms, t the time, Δt the timestep, t_{tot} the total simulation time, $N_{\Delta t}$ the total number of time steps, $\mathbf{r}_{i,\mathrm{xy}}(t)$ the position vector of the atom i with x and y components, respectively.

Using the MSD values obtained, the surface diffusivity is calculated by fitting the least squares to Eq. 5. To isolate surface diffusion effects, the dimensionality is fixed at 2. The MSD data are truncated between 10% and 70% of the total simulation time to avoid potential noise in the early stages and the effect of fewer samples at later stages.

$$D = \frac{\mathrm{MSD}(\Delta t)}{2d\Delta t} + D_{\mathrm{offset}} \tag{5}$$

The results of diffusivity calculations through MD simulations indicate that the SevenNet-0 generally underestimates diffusivity values compared to DFT (Fig. 6). However, the fine-tuned NNP shows improvements in the overall distribution of diffusivity values. At a temperature of 350 K, the fine-tuned NNP completely covers

the diffusivity range of DFT, while SevenNet-0 almost misses the diffusivity range of DFT. Here, the average diffusivity value of the fine-tuned NNP is much closer to that of DFT, while SevenNet-0 shows much larger differences. At a temperature of 300 K, this trend becomes slightly weaker, but the still fine-tuned NNP shows an average value closer to DFT, compared to SevenNet-0. At a temperature of 250 K, the diffusivity distribution of the SevenNet-0 does not overlap with that of DFT at all, whereas the fine-tuned NNP partially covers the DFT diffusivity range.

To further investigate the discrepancies in diffusivity distributions between the DFT and NNP results at 250 K, HF trajectories were analyzed from their initial positions for the cases with highest and lowest diffusivity (Fig. S2). Overall, NNP trajectories showed a greater tendency for molecules to remain near their initial positions compared to DFT, a trend observed in both the SevenNet-0 and fine-tuned NNP models. This discrepancy may be attributed to several factors such as finite-size effects arising from the small cell size used for comparison with DFT, the relatively short MD simulation time of 10 ps, and the insufficient sampling of HF diffusivity due to the limited number of ensembles.

Furthermore, the fine-tuned NNP model exhibits a larger spread in fast and slow diffusion events compared to SevenNet-0. This spread originates from variations in HF molecular movement across different MD runs. In particular, some HF molecules, especially those positioned near the topmost layers with higher mobility, show significantly greater displacement in certain simulations but remain nearly immobile in others. Conversely, when HF molecules do not exhibit significant displacement from their initial positions, the results from SevenNet-0 and the fine-tuned NNP closely overlap, suggesting that both models capture slow diffusion cases in a similar manner. Given the limited cell size and short MD duration, these factors contribute to the observed spread in diffusion behavior. Although increasing the simulation time and system size would help reduce noise, we maintain these parameters to ensure consistency with the DFT simulations.

Additionally, to assess the extrapolation capability of the fine-tuned NNP model in larger systems, we perform MD simulations at 400 K using a system with lateral dimensions three times larger than the original cell. As shown in Fig. S3, the overall energy-per-atom trend remains consistent between the small and large systems, with reduced fluctuations in the larger system. This suggests that the fine-tuned model successfully generalizes to larger-scale simulations despite differences in periodic boundary conditions.

3.3. Analysis of diffusion behaviors

To investigate the impact of IF_5 additives on the surface diffusion of HF etchants, NVT MD simulations of 1 ML HF are conducted with and without the presence of 1 ML IF_5 using the fine-tuned NNP. The results, shown in Fig. 7, indicate that the diffusivity of HF increases at low temperatures when IF_5 is present. Furthermore, the diffusion

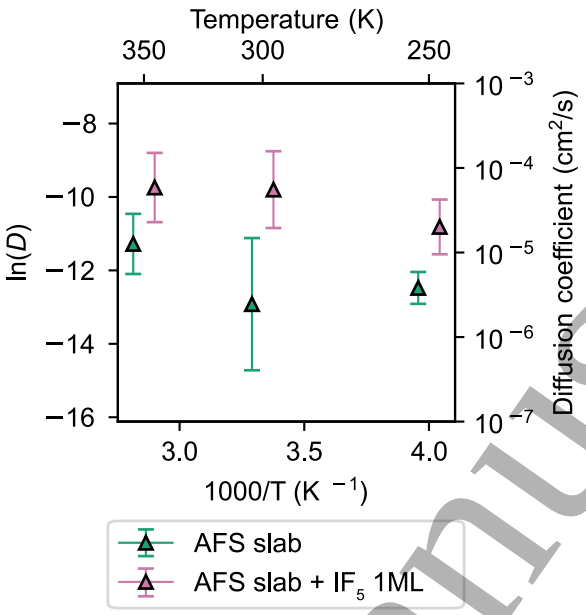

Figure 7. Effect of IF_5 on diffusivity of HF molecules using fine-tuned NNP. NVT MD simulations are performed for 10 ps at temperatures of 250, 300, and 350 K, with five simulations conducted at each temperature. Markers represent the average value of $\ln(D)$, while solid lines show the range between the minimum and maximum values. For clarity, results obtained at the same temperature using different systems (AFS slab and AFS slab+IF_5 1ML) are slightly shifted laterally in the diagram.

barrier is found to decrease from 0.097 to 0.079 eV.

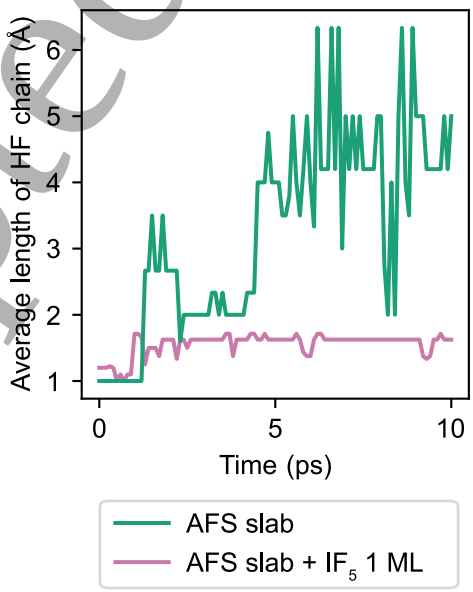

Figure 8. Average length of HF chain during MD using fine-tuned NNP.

To understand the mechanistic origins of this phenomenon, changes in the length of

the HF chain are analyzed during the MD process at 250 K (Fig. 8). To define the HF chain in the given system, HF molecules are first identified and the nearest neighbors H and F of each HF molecule are examined. If both nearest neighbors are HF molecules, it is classified as part of a chain; if one or more neighbors are NH_4^+, SiF_6^{2-}, or IF_5, it is classified as a node. The criterion for hydrogen bonding between HF molecules is set at 1.9 times the equilibrium length of the HF bond. The length of the HF chain is defined as the total number of HF molecules connecting one node to another.

It is well known that HF molecules in the liquid state tend to form one-dimensional chains through intermolecular bonding [60, 61]. When only 1 ML of HF is present, the average chain length at 250 K exceeds 3, forming relatively long chains similar to those in the liquid state. In contrast, when IF_5 is present, HF molecules can also form H–F bonds with IF_5, resulting in shorter average chain lengths. HF molecules in shorter chains, especially those not bonded to other HF molecules, can break their relatively weaker bonds with IF_5 easily and move more freely. This explains the observed increase in diffusivity under these conditions.

4. Conclusion

In this study, our objective was to construct an NNP to provide an enhanced atomistic understanding of the diffusion of HF on AFS surfaces, a critical process in cryogenic plasma etching for 3D NAND flash memory fabrication. Using the pretrained SevenNet-0 model as a foundation, we developed a fine-tuned NNP tailored to accurately simulate HF diffusion dynamics. Starting from the pretrained SevenNet-0 model parameters, we successfully developed a stable and accurate NNP capable of reliably simulating the diffusion process even with a limited amount of training data. By fine-tuning the model with a minimal dataset from DFT calculations, we achieved substantial improvements in accuracy for atomic configurations encountered during the diffusion process. Notably, the fine-tuned model reduced the energy RMSE from approximately 24 meV/atom (as seen in the scratch NNP) to around 1 meV/atom, highlighting a significant enhancement in predictive performance. Compared to the scratch NNP, the fine-tuned model demonstrated superior stability and accuracy in MD simulations, effectively capturing surface diffusion behaviors even with limited training data.

Our analysis revealed that the presence of additive gases like IF_5 enhances HF diffusivity by reducing chain formation and lowering the diffusion barrier, facilitating more effective etching. These findings highlight the potential of fine-tuned NNPs as a computationally efficient surrogate model for modeling complex surface interactions and diffusion behavior in cryogenic etching processes, providing valuable insights into semiconductor process modeling.

5. Acknowledgments

This work was supported by Samsung Electronics Co., Ltd (IO240222-09079-01). The computations were carried out at the Korea Institute of Science and Technology Information (KISTI) National Supercomputing Center (KSC-2024-CRE-0215).

6. Data availability statement

All data that support the findings of this study are openly available at the following URL/DOI: `https://github.com/HyungminAn/LowTempEtch.git`.

7. Reference

[1] J C Arnold and H H Sawin. Charging of pattern features during plasma etching. *Journal of Applied Physics*, 70(10):5314–5317, 1991.

[2] N. R. Rueger, M. F. Doemling, M. Schaepkens, J. J. Beulens, T. E. F. M. Standaert, and G. S. Oehrlein. Selective etching of SiO_2 over polycrystalline silicon using CHF_3 in an inductively coupled plasma reactor. *Journal of Vacuum Science & Technology A: Vacuum, Surfaces, and Films*, 17(5):2492–2502, 1999.

[3] F. Gaboriau, G. Cartry, M-C. Peignon, and Ch. Cardinaud. Selective and deep plasma etching of SiO_2: Comparison between different fluorocarbon gases (CF_4, C_2F_6, CHF_3) mixed with CH_4 or H_2 and influence of the residence time. *Journal of Vacuum Science & Technology B: Microelectronics and Nanometer Structures Processing, Measurement, and Phenomena*, 20(4):1514–1521, 2002.

[4] Rino Micheloni, Luca Crippa, Cristian Zambelli, and Piero Olivo. Architectural and integration options for 3D NAND flash memories. *Computers*, 6(3):27, 2017.

[5] Geun Ho Lee, Sungmin Hwang, Junsu Yu, and Hyungjin Kim. Architecture and process integration overview of 3D NAND flash technologies. *Applied Sciences*, 11(15):6703, 2021.

[6] Hye Joo Lee, Hyun Woo Tak, Seong Bae Kim, Seul Ki Kim, Tae Hyun Park, Ji Yeun Kim, Dain Sung, Wonseok Lee, Seung Bae Lee, Keunsuk Kim, Byeong Ok Cho, Young Lea Kim, Ki Chan Lee, Dong Woo Kim, and Geun Young Yeom. Characteristics of high aspect ratio SiO_2 etching using $C_4H_2F_6$ isomers. *Applied Surface Science*, 639:158190, 2023.

[7] Robert J Hoekstra, Mark J Kushner, Valeriy Sukharev, and Phillipe Schoenborn. Microtrenching resulting from specular reflection during chlorine etching of silicon. *Journal of Vacuum Science & Technology B: Microelectronics and Nanometer Structures Processing, Measurement, and Phenomena*, 16(4):2102–2104, 1998.

[8] R Dussart, T Tillocher, P Lefaucheux, and M Boufnichel. Plasma cryogenic etching of silicon: from the early days to today's advanced technologies. *Journal of Physics D: Applied Physics*, 47(12):123001, 2014.

[9] G. Antoun, T. Tillocher, A. Girard, P. Lefaucheux, J. Faguet, H. Kim, D. Zhang, M. Wang, K. Maekawa, C. Cardinaud, and R. Dussart. Cryogenic nanoscale etching of silicon nitride selectively to silicon by alternating SiF_4/O_2 and Ar plasmas. *Journal of Vacuum Science & Technology A: Vacuum, Surfaces, and Films*, 40(5):052601, 2022.

[10] Shih-Nan Hsiao, Makoto Sekine, Nikolay Britun, Michael K. T. Mo, Yusuke Imai, Takayoshi Tsutsumi, Kenji Ishikawa, Yuki Iijima, Ryutaro Suda, Masahiko Yokoi, Yoshihide Kihara, and Masaru Hori. Pseudo-Wet plasma mechanism enabling high-throughput dry etching of SiO_2 by cryogenic-assisted surface reactions. *Small Methods*, page e2400090, 2024.

[11] Meihua Shen, Thorsten Lill, John Hoang, Hao Chi, Aaron Routzahn, Jonathan Church, Pramod Subramonium, Ragesh Puthenkovilakam, Sirish Reddy, Sonal Bhadauriya, et al. Progress report

on high aspect ratio patterning for memory devices. *Japanese Journal of Applied Physics*, 62(SI):SI0801, 2023.

[12] Thorsten Lill, Mingmei Wang, Dongjun Wu, Youn-Jin Oh, Tae Won Kim, Mark Wilcoxson, Harmeet Singh, Vahid Ghodsi, Steven M George, Yuri Barsukov, et al. Low-temperature etching of silicon oxide and silicon nitride with hydrogen fluoride. *Journal of Vacuum Science & Technology A*, 42(6), 2024.

[13] Stefan Tinck, Erik C. Neyts, and Annemie Bogaerts. Fluorine–silicon surface reactions during cryogenic and near room temperature etching. *The Journal of Physical Chemistry C*, 118(51):30315–30324, 2014.

[14] G. Antoun, T. Tillocher, P. Lefaucheux, J. Faguet, K. Maekawa, and R. Dussart. Mechanism understanding in cryo atomic layer etching of SiO_2 based upon C_4F_8 physisorption. *Scientific Reports*, 11(1):357, 2021.

[15] Shih-Nan Hsiao, Makoto Sekine, Kenji Ishikawa, Yuki Iijima, Yoshinobu Ohya, and Masaru Hori. An approach to reduce surface charging with cryogenic plasma etching using hydrogen-fluoride contained gases. *Applied Physics Letters*, 123(21):212106, 2023.

[16] Thorsten Lill, Ivan L. Berry, Meihua Shen, John Hoang, Andreas Fischer, Theo Panagopoulos, Jane P. Chang, and Vahid Vahedi. Dry etching in the presence of physisorption of neutrals at lower temperatures. *Journal of Vacuum Science & Technology A*, 41(2):023005, 2023.

[17] Yoshihide Kihara, Maju Tomura, Wataru Sakamoto, Masanobu Honda, and Masayuki Kojima. Beyond 10 μm depth ultra-high speed etch process with 84% lower carbon footprint for memory channel hole of 3D NAND flash over 400 layers. *2023 IEEE Symposium on VLSI Technology and Circuits (VLSI Technology and Circuits)*, 00:1–2, 2023.

[18] You Jung Gill, Doo San Kim, Hong Seong Gil, Ki Hyun Kim, Yun Jong Jang, Ye Eun Kim, and Geun Young Yeom. Cyclic etching of silicon oxide using NF_3/H_2 remote plasma and NH_3 gas flow. *Plasma Processes and Polymers*, 18(11), 2021.

[19] Romel Hidayat, Khabib Khumaini, Hye-Lee Kim, Tanzia Chowdhury, Tirta Rona Mayangsari, Seongjae Cho, Byungchul Cho, Sangjoon Park, Jongwan Jung, and Won-Jun Lee. Gas-phase etching mechanism of silicon oxide by a mixture of hydrogen fluoride and ammonium fluoride: A density functional theory study. *Journal of Vacuum Science & Technology A*, 41(3):032604, 2023.

[20] Khabib Khumaini, Yewon Kim, Romel Hidayat, Tanzia Chowdhury, Hye-Lee Kim, Byungchul Cho, Sangjoon Park, and Won-Jun Lee. Etching mechanism of amorphous hydrogenated silicon nitride by hydrogen fluoride. *Applied Surface Science*, 654:159414, 2024.

[21] Jong Woo Kim, Seok Jin Ryu, Young Chul Lee, Hyun Myung Yang, and Hyeok Beom Shin. Electronic devices having improved light extraction efficiency and methods for manufacturing the same, October 2018. Filed under US Patent Application Publication.

[22] Gaelle Antoun, Rémi Dussart, Thomas Tillocher, Philippe Lefaucheux, Christophe Cardinaud, Aurélie Girard, Shigeru Tahara, Kumiko Yamazaki, Koichi Yatsuda, Jacques Faguet, et al. The role of physisorption in the cryogenic etching process of silicon. *Japanese Journal of Applied Physics*, 58(SE):SEEB03, 2019.

[23] Yehya Haidar, Ahmed Rhallabi, Amand Pateau, Arezki Mokrani, Fadia Taher, Fabrice Roqueta, and Mohamed Boufnichel. Simulation of cryogenic silicon etching under $SF_6/O_2/Ar$ plasma discharge. *Journal of Vacuum Science & Technology A*, 34(6), 2016.

[24] G Marcos, A Rhallabi, and P Ranson. Topographic and kinetic effects of the SF_6/O_2 rate during a cryogenic etching process of silicon. *Journal of Vacuum Science & Technology B: Microelectronics and Nanometer Structures Processing, Measurement, and Phenomena*, 22(4):1912–1922, 2004.

[25] Chad M Huard, Yiting Zhang, Saravanapriyan Sriraman, Alex Paterson, and Mark J Kushner. Role of neutral transport in aspect ratio dependent plasma etching of three-dimensional features. *Journal of Vacuum Science & Technology A*, 35(5), 2017.

[26] Theodoros Panagopoulos and Thorsten Lill. Neutral transport during etching of high aspect ratio

features. *Journal of Vacuum Science & Technology A*, 41(3), 2023.

[27] Patrick Vanraes, Syam Parayil Venugopalan, Matthieu Besemer, and Annemie Bogaerts. Assessing neutral transport mechanisms in aspect ratio dependent etching by means of experiments and multiscale plasma modeling. *Plasma Sources Science and Technology*, 32(6):064004, 2023.

[28] Graeme Henkelman, Blas P. Uberuaga, and Hannes Jónsson. A climbing image nudged elastic band method for finding saddle points and minimum energy paths. *The Journal of Chemical Physics*, 113(22):9901–9904, 12 2000.

[29] Graeme Henkelman and Hannes Jónsson. Improved tangent estimate in the nudged elastic band method for finding minimum energy paths and saddle points. *The Journal of Chemical Physics*, 113(22):9978–9985, 12 2000.

[30] Yutack Park, Jaesun Kim, Seungwoo Hwang, and Seungwu Han. Scalable parallel algorithm for graph neural network interatomic potentials in molecular dynamics simulations. *Journal of Chemical Theory and Computation*, 2024.

[31] Bowen Deng, Peichen Zhong, KyuJung Jun, Janosh Riebesell, Kevin Han, Christopher J. Bartel, and Gerbrand Ceder. CHGNet as a pretrained universal neural network potential for charge-informed atomistic modelling. *Nat. Mach. Intell.*, 5(9):1031–1041, 2023.

[32] Chi Chen and Shyue Ping Ong. A universal graph deep learning interatomic potential for the periodic table. *Nature Computational Science*, 2(11):718–728, 2022.

[33] Ilyes Batatia, Philipp Benner, Yuan Chiang, Alin M Elena, Dávid P Kovács, Janosh Riebesell, Xavier R Advincula, Mark Asta, Matthew Avaylon, William J Baldwin, et al. A foundation model for atomistic materials chemistry. *arXiv preprint arXiv:2401.00096*, 2023.

[34] Changho Hong, Jaehoon Kim, Jaesun Kim, Jisu Jung, Suyeon Ju, Jeong Min Choi, and Seungwu Han. Applications and training sets of machine learning potentials. *Sci. Technol. Adv. Mater.: Methods*, 3(1):2269948, 2023.

[35] Christian M. Clausen, Jan Rossmeisl, and Zachary W. Ulissi. Adapting OC20-trained EquiformerV2 models for high-entropy materials, 2024.

[36] Bowen Deng, Yunyeong Choi, Peichen Zhong, Janosh Riebesell, Shashwat Anand, Zhuohan Li, KyuJung Jun, Kristin A. Persson, and Gerbrand Ceder. Overcoming systematic softening in universal machine learning interatomic potentials by fine-tuning, 2024.

[37] MDIL-SNU. SevenNet GitHub Repository, 2024. Accessed: 2024-12-10.

[38] Simon Batzner, Albert Musaelian, Lixin Sun, Mario Geiger, Jonathan P Mailoa, Mordechai Kornbluth, Nicola Molinari, Tess E Smidt, and Boris Kozinsky. E (3)-equivariant graph neural networks for data-efficient and accurate interatomic potentials. *Nature communications*, 13(1):2453, 2022.

[39] Anubhav Jain, Shyue Ping Ong, Geoffroy Hautier, Wei Chen, William Davidson Richards, Stephen Dacek, Shreyas Cholia, Dan Gunter, David Skinner, Gerbrand Ceder, et al. Commentary: The Materials Project: A materials genome approach to accelerating materials innovation. *APL materials*, 1(1), 2013.

[40] Amil Merchant, Simon Batzner, Samuel S Schoenholz, Muratahan Aykol, Gowoon Cheon, and Ekin Dogus Cubuk. Scaling deep learning for materials discovery. *Nature*, 624(7990):80–85, 2023.

[41] Janosh Riebesell, Rhys EA Goodall, Anubhav Jain, Philipp Benner, Kristin A Persson, and Alpha A Lee. Matbench Discovery–An evaluation framework for machine learning crystal stability prediction. *arXiv preprint arXiv:2308.14920*, 2023.

[42] Georg Kresse and Jürgen Furthmüller. Efficient iterative schemes for ab initio total-energy calculations using a plane-wave basis set. *Physical review B*, 54(16):11169, 1996.

[43] John P Perdew, Kieron Burke, and Matthias Ernzerhof. Generalized gradient approximation made simple. *Physical review letters*, 77(18):3865, 1996.

[44] Aidan P Thompson, H Metin Aktulga, Richard Berger, Dan S Bolintineanu, W Michael Brown, Paul S Crozier, Pieter J In't Veld, Axel Kohlmeyer, Stan G Moore, Trung Dac Nguyen, et al. LAMMPS-a flexible simulation tool for particle-based materials modeling at the atomic, meso,

and continuum scales. *Computer Physics Communications*, 271:108171, 2022.

[45] Ask Hjorth Larsen, Jens Jørgen Mortensen, Jakob Blomqvist, Ivano E Castelli, Rune Christensen, Marcin Dułak, Jesper Friis, Michael N Groves, Bjørk Hammer, Cory Hargus, et al. The atomic simulation environment—a Python library for working with atoms. *Journal of Physics: Condensed Matter*, 29(27):273002, 2017.

[46] Stefan Grimme, Jens Antony, Stephan Ehrlich, and Helge Krieg. A consistent and accurate ab initio parametrization of density functional dispersion correction (DFT-D) for the 94 elements H-Pu. *The Journal of chemical physics*, 132(15), 2010.

[47] Stefan Grimme, Stephan Ehrlich, and Lars Goerigk. Effect of the damping function in dispersion corrected density functional theory. *Journal of computational chemistry*, 32(7):1456–1465, 2011.

[48] Elmer O Schlemper, Walter C Hamilton, and JJ Rush. Structure of cubic ammonium fluosilicate: Neutron-diffraction and neutron-inelastic-scattering studies. *The Journal of Chemical Physics*, 44(6):2499–2505, 1966.

[49] EO Schlemper and Walter C Hamilton. On the structure of trigonal ammonium flourosilicate. *The Journal of Chemical Physics*, 45(1):408–409, 1966.

[50] Jan Fábry, Jindřich Chval, and Václav Petříček. A new modification of diammonium hexafluorosilicate,(NH_4) $2SiF_6$. *Acta Crystallographica Section E: Structure Reports Online*, 57(10):i90–i91, 2001.

[51] Nobuya Miyoshi, Hiroyuki Kobayashi, Kazunori Shinoda, Masaru Kurihara, Kohei Kawamura, Yutaka Kouzuma, and Masaru Izawa. Atomic layer etching of sio2 with self-limiting behavior on the surface modification step using sequential exposure of hf and nh3. *Journal of Vacuum Science & Technology A*, 40(1), 2022.

[52] Leandro Martínez, Ricardo Andrade, Ernesto G Birgin, and José Mario Martínez. PACKMOL: A package for building initial configurations for molecular dynamics simulations. *Journal of computational chemistry*, 30(13):2157–2164, 2009.

[53] Jisu Jung, Suyeon Ju, Purun-hanul Kim, Deokgi Hong, Wonseok Jeong, Jinhee Lee, Seungwu Han, and Sungwoo Kang. Electrochemical degradation of Pt_3Co nanoparticles investigated by off-lattice kinetic Monte Carlo simulations with machine-learned Potentials. *ACS Catalysis*, 13(24):16078–16087, 2023.

[54] Changho Hong, Sangmin Oh, Hyungmin An, Purun-hanul Kim, Yaeji Kim, Jae-hyeon Ko, Jiwoong Sue, Dongyean Oh, Sungkye Park, and Seungwu Han. Atomistic Simulation of HF Etching Process of Amorphous Si_3N_4 Using Machine Learning Potential. *ACS Applied Materials & Interfaces*, 16(36):48457–48469, 2024. PMID: 39198036.

[55] Jisu Jung, Hyungmin An, Jinhee Lee, and Seungwu Han. Modified Activation-Relaxation Technique (ARTn) Method Tuned for Efficient Identification of Transition States in Surface Reactions. *Journal of Chemical Theory and Computation*, 20(18):8024–8034, 2024. PMID: 39240127.

[56] T Hattori, H Kobayashi, H Ohtake, K Akinaga, Y Kurosaki, A Takei, A Sekiguchi, K Maeda, C Takubo, and M Yamada. Highly selective isotropic gas-phase etching of SiO_2 using HF and methanol at temperatures–30° C and lower. *Japanese Journal of Applied Physics*, 62(SI):SI1001, 2023.

[57] Shih-Nan Hsiao, Nikolay Britun, Takayoshi Tsutsumi, Kenji Ishikawa, Makoto Sekine, Masaru Hori, et al. Manipulation of etch selectivity of silicon nitride over silicon dioxide to a-carbon by controlling substrate temperature with a CF_4/H_2 plasma. *Vacuum*, 210:111863, 2023.

[58] Tokuhisa Ohiwa, Keiji Horioka, Tsunetoshi Arikado, Isahiro Hasegawa, and Haruo Okano Haruo Okano. SiO_2 tapered etching employing magnetron discharge of fluorocarbon gas. *Japanese journal of applied physics*, 31(2R):405, 1992.

[59] Xingfeng He, Yizhou Zhu, Alexander Epstein, and Yifei Mo. Statistical variances of diffusional properties from ab initio molecular dynamics simulations. *npj Computational Materials*, 4(1):18, 2018.

[60] Sylvia E McLain, Chris J Benmore, Joan E Siewenie, Jacob Urquidi, and John FC Turner. On

the structure of liquid hydrogen fluoride. *Angewandte Chemie*, 116(15):1986–1989, 2004.

[61] Pal Jedlovszky Renzo Vallauri. Structural properties of liquid HF: a computer simulation investigation. *Molecular Physics*, 93(1):15–24, 1998.